Fundamental Research 2 (2022) 619–628

Contents lists available at ScienceDirect

Fundamental Research

journal homepage: http://www.keaipublishing.com/en/journals/fundamental-research/

Article

Stretchable graded multichannel self-powered respiratory sensor inspired by shark gill

Yang Zou[a,b,1], Yansong Gai[b,c,1], Puchuan Tan[b,d], Dongjie Jiang[b,e], Xuecheng Qu[b,e], Jiangtao Xue[a,b], Han Ouyang[d,e], Bojing Shi[d], Linlin Li[b,e], Dan Luo[b,e], Yulin Deng[a,*], Zhou Li[b,c,e,*], Zhong Lin Wang[b,c,e]

[a] School of Life Science, Institute of Engineering Medicine, Beijing Institute of Technology, Beijing 100081, China
[b] CAS Center for Excellence in Nanoscience, Beijing Key Laboratory of Micro-Nano Energy and Sensor, Beijing Institute of Nanoenergy and Nanosystems, Chinese Academy of Sciences, Beijing 101400, China
[c] Center on Nanoenergy Research, School of Chemistry and Chemical Engineering, School of Physical Science and Technology, Guangxi University, Nanning 530004, China
[d] Key Laboratory for Biomechanics and Mechanobiology of Chinese Education Ministry, Beijing Advanced Innovation Centre for Biomedical Engineering, School of Biological Science and Medical Engineering, Beihang University, Beijing 100083, China
[e] School of Nanoscience and Technology, University of Chinese Academy of Sciences, Beijing 100049, China

ARTICLE INFO

Article history:
Received 9 October 2021
Received in revised form 5 December 2021
Accepted 14 January 2022
Available online 25 January 2022

Keywords:
Bionic
Shark gill
Graded
Multichannel
Respiratory sensing

ABSTRACT

Respiratory sensing provides a simple, non-invasive, and efficient way for medical diagnosis and health monitoring, but it relies on sensors that are conformal, accurate, durable, and sustainable working. Here, a stretchable, multichannel respiratory sensor inspired by the structure of shark gill cleft is reported. The bionic shark gill structure can convert transverse elastic deformation into longitudinal elastic deformation during stretching. Combining the optimized bionic shark gill structure with the piezoelectric and the triboelectric effect, the bionic shark gill respiratory sensor (BSG-RS) can produce a graded electrical response to different tensile strains. Based on this feature, BSG-RS can simultaneously monitor the breathing rate and breathing depth of the human body accurately, and realize the effective recognition of the different human body's breathing state under the supporting software. With good stretchability, wearability, accuracy, and long-term stability (50,000 cycles), BSG-RS is expected to be applied as self-powered smart wearables for mobile medical diagnostic analysis in the future.

1. Introduction

With the aging of the global population and the aggravation of air pollution, the prevalence of various respiratory diseases continues to rise [1,2]. Particularly at the moment, COVID-19 is raging around the world. There is a huge demand for equipment to detect respiratory abnormalities [3]. Clinical respiratory system detection mainly includes medical imaging, pulmonary function test, and auscultation [4]. These clinical medical tests usually require expensive medical testing equipment or professional physician guidance [5,6]. In contrast, the detection of human respiratory movement is relatively easy. The respiratory movement of the human body contains important physiological information, including breathing frequency and breathing depth, which can provide critical indicators for predicting or diagnosing potential respiratory diseases such as chronic obstructive pulmonary disease and respiratory dysfunction caused by cystic fibrosis [7–9]. For some people with a potential risk of chronic diseases, long-term and continuous monitoring of respiratory status is required, which inconveniences both patients and doctors. In addition, some respiratory diseases such as COVID-19 and tuberculosis are highly infectious, so remote detection and diagnosis are of great importance [10,11]. It is highly urgent to develop a wearable respiratory sensing system with low power consumption, high monitoring accuracy and comfort [12].

The piezoelectric nanogenerator (PENG) and triboelectric nanogenerator (TENG) can convert the mechanical energy of the human body into electricity [13–16], which can be used as an ideal active sensor to monitor the respiratory movement of the human body without the need for an external power supply. Liu et al. proposed a piezoelectric active sensor for respiratory sensing based on an electrospinning PVDF film [17]. Zhang et al. reported a lateral sliding mode TENG to monitor respiratory rate by sensing the change of abdominal circumference when

* Corresponding authors.
E-mail addresses: deng@bit.edu.cn (Y. Deng), zli@binn.cas.cn (Z. Li).
[1] These authors contributed equally to this work.

https://doi.org/10.1016/j.fmre.2022.01.003

breathing [18]. A washable fabric-based TENG was developed and integrated with a chest strap to detect the movement of the chest during breathing [19]. A noncontact self-powered pressure sensing bed sheet with a flexible hollow microstructure was also designed to detect continuous respiratory signals and transmit them to a mobile phone wirelessly [20]. These respiratory sensors based on TENG and PENG have greatly promoted self-powered wearable devices for physiological signal monitoring. However, current devices still face some challenges in practical use. The first is that the sensing units do not match the modulus of human tissue. The design of sensing units with comparable mechanical properties of human tissue can better respond to the mechanical displacement caused by respiration, reduce mechanical energy loss, and improve the comfort of human wearing [21,22]. The second is that the sensors may be interfered by other body movements during respiratory monitoring. The high sensitivity makes the sensors generate electrical signals from all perceptible body movements, which may disturb the target signal [23]. The third is the accuracy and stability of the sensors under long-term monitoring. Especially for chronic respiratory diseases, long-term respiratory monitoring has specific requirements for sensors in terms of fatigue resistance and stability [24,25].

Gills are the respiratory organs of fish to enable gas exchange underwater. Shark is a cartilaginous fish with soft and elastic gill cleft structure compared to the hard gill cover of bony fish. There are pairs of almost parallel gill clefts on each side of the shark. With these gill clefts, sharks can maintain effective breathing while swimming in the sea. This work proposes an elastic deformation structure inspired by the shark gill cleft, which can transform transverse deformation into longitudinal deformation under stretching. Based on the bionic shark gill (BSG) structure, a stretchable shark gill-like nanogenerator is constructed by combining the triboelectric and piezoelectric effects. After optimizing the BSG structure, a graded response to tensile strain is achieved. A stretchable multichannel respiratory sensor is further fabricated based on the optimized BSG structure. The bionic shark gill respiratory sensor (BSG-RS) can simultaneously monitor the respiratory rate and respiratory depth by perceiving the changes in the human body's abdominal circumference or chest circumference. In addition, a wearable wireless real-time respiratory monitoring and analysis system is developed by integrating BSG-RS with a wireless signal transmission module and a supporting software based on pattern recognition algorithm, which can realize real-time monitoring of breathing movement under different postures and identifying different breathing states according to the signals recorded in multiple channels.

2. Material and methods

Fabrication of BSG structure: The molds of the BSG structure were prepared by 3D printing polylactic acid (Raise 3D Technologies), including an upper layer with strip grooves and a flat substrate layer. The silicone (Ecoflex TM 00–30, Smooth-On, Inc.) consisting of Part A and Part B was mixed thoroughly (1:1 by weight), poured into the molds, and placed in a vacuum drying chamber 3 min to remove bubbles. After curing at 50 ˚C for 2 h, the silicone was peeled off from the molds, and the upper and substrate layers of the BSG structure were obtained. The PDMS (Dow corning, Sylgard 184) main agents and curing agents (10:1 by weight) were mixed thoroughly and vacuum degassed for 30 min before filled the strip grooves of the upper layer. After curing at 80 ˚C for 4 h, the upper layer was overlapped with the substrate layer, and the edges were encapsulated together with a preformed gel of silicone. Finally, curing at 50 ˚C for 2 h, the BSG structure was completed.

Fabrication of BSG nanogenerator: The BSG nanogenerator was fabricated on the basis of the BSG structure. For BSG-PENG, a commercial Metallized Piezo Film Sheet (Measurement Specialties, Inc., TE Connectivity company.) was cut as the size of the strip groove in the upper layer of the BSG structure. Then the piezoelectric strips connected with the varnished wire were placed in grooves and filled with PDMS. After curing at 80 ˚C for 4 h and assembling with the substrate layer, the BSG-PENG was fabricated. For BSG-TENG, the copper tapes connected with varnished wire were fixed to the bottom of the strips in the upper layer of BSG structure. Then a substrate layer with a groove (the same size as the functional area of the upper layer) is prepared to fill with the AgNWs and cover by silicone. After assembling the upper layer with the substrate layer, the BSG-TENG was fabricated. For BSG-PTNG, the same upper layer as BSG-PENG was prepared. Then, a substrate layer similar to BSG-TENG was prepared for coating the AgNWs to the surface rather than the interior. After assembling the upper layer with the substrate layer, the BSG-PTNG was fabricated.

Fabrication of BSG-RS: The entire fabrication process of BSG-RS is shown in Fig. S1. BSG-RS was fabricated based on an optimized BSG structure and BSG-PTNG. The length of the middle strip in the upper layer of BSG-RS was set as 35 mm, and the lengths of the strips on both sides decreased to 30 mm, 25 mm and 20 mm, respectively. The width of all strips was set as 6 mm, the thickness was set as 2 mm (composed of 1 mm silicone layer, 1 mm PDMS layer and 122 μm piezo film sheet), and the spacing between strips was set as 1 mm. The thickness of the silicone substrate was set as 2 mm. The dimensions of the entire BSG-RS were 90 mm × 50 mm × 4 mm.

Construction of wireless real-time respiratory monitoring and analysis system: The wireless real-time respiratory monitoring and analysis system was constructed by a BSG-RS, a multichannel wireless signal acquisition/ transmission module (including an OpenBCI 8 bit Board and an OpenBCI programmable dongle), a laptop, and supporting software. The BSG-RS was connected with the OpenBCI 8 bit Board to capture and transmit respiratory signals of the human body. The OpenBCI programmable dongle was connected with the laptop to receive signals. The supporting software was used to display the real-time respiratory signals (including respiratory waveforms, respiratory depth and respiratory rate), record and analyze the relevant data.

Development of supporting software: The supporting software was developed based on Python 3.8 and Pycharm to real-time analyze the collected data and judge the breathing state. There are five steps: (1) First, call the Serial module to communicate with OpenBCI and read information in real-time. (2) Call the Butterworth low-pass filter of the Signal module to perform preliminary data filtering (up to the frequency of 3.6Hz). Then, the low-frequency information of the signal (0.2Hz) is extracted and subtracted to complete the baseline repair. (3) According to the Matplotlab.Pyplot module, the signal images of seven channels are plotted with a fixed time length. Meanwhile, normalize the signal to the interval of (0, 256), set the Colormap to Reds and map the real-time signal to the interval. The color block contrast images are plotted according to the real-time signal intensity. The images are transmitted to the software's interface in real-time through the Tkinter module, and the FPS is set to 30. (4) Use the sliding window to intercept the signal of the effective interval. (5) Search the peak, calculate the peak-valley value and the peak position. Extract the amplitude and frequency of the segment of data according to these values. Judge the breathing state according to the set breathing depth/rate interval, and transmit to the display interface. Other Python library calls include Numpy, Pandas, Random, and Scipy.

Characterization and measurement: The SEM images were taken by a field-emission scanning electron microscope (Hitachi SU8020). An electric vertical test bench (ESM301/Mark-10) was used for the mechanical tensile test, and a force gauge (Mark-10/M5) was used to detect the tensile force. A fixed position digital camera was used to take photos of the BSG structures under different tensile strains, and the arch heights of different strips in the optical photos were counted by ImageJ Pro, error bars were calculated using mean ± SD. with a group size n ≥ 3. A linear motor (LinMot E1100) was used to apply periodic tensile loads on devices. Different working frequencies and tensile strains were achieved by adjusting the displacement, velocity, and acceleration of the linear motor. An electrometer (Keithley 6517) was used to measure the I_{SC} and Q_{SC}. An oscilloscope (Teledyne LeCroy DPO6450) was used to measure the V_{OC}.

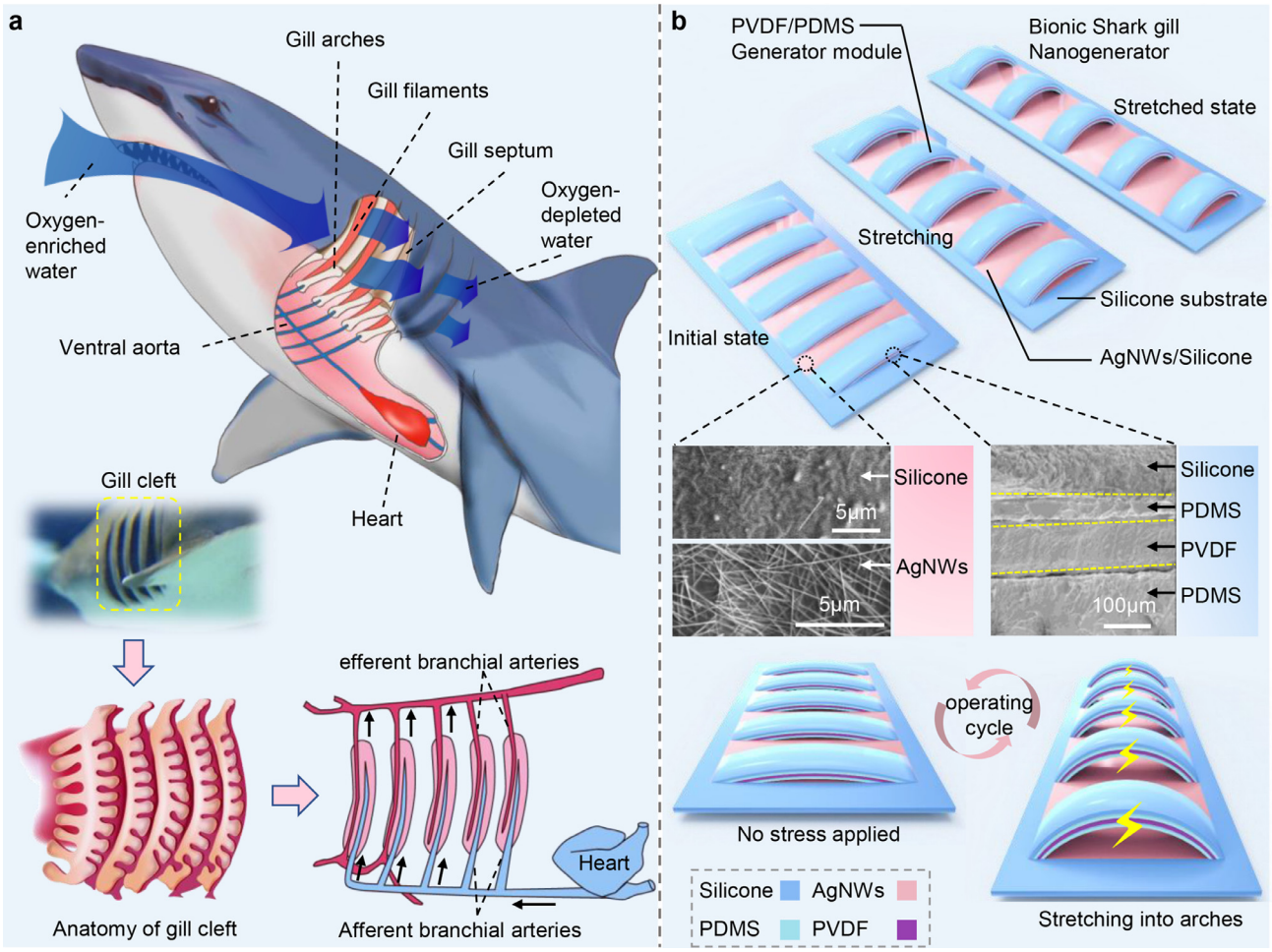

Fig. 1. Bionic principle and structure of bionic shark gill nanogenerator. (a) Schematic diagram of the shark's respiratory system and the anatomy of gill cleft. (b) Schematic diagram of bionic shark gill nanogenerator in different stretched states.

3. Results and discussion

3.1. Bionic principle and structure of shark gill-like nanogenerator

Biological structures in nature often contain a lot of wisdom [26,27]. Here, the gill structure of a shark brings us inspiration for the design of a stretchable self-powered multichannel biosensor. The gill of sharks is mainly composed of gill arch, gill filament, gill septum and gill pouch [28]. The respiration of sharks mainly depends on the gill cleft structure on both sides of the head, usually with five to seven on each side (Fig. 1a). The opening and closing of several pairs of gill clefts are synchronized under the coordinated control of branchial muscle groups when shark breathing [29]. More details on the structure and operation of shark gill tissue are provided in Note S1.

By imitating the gill cleft structure of the shark, we designed an elastic deformation structure and constructed it into a stretchable multichannel nanogenerator (Fig. 1b). The device can be divided into two layers according to its function. The upper layer is the main functional layer, consisting of several parallel strip-shaped power generation units. Each power generation unit is a sandwich structure consisted of silicone, polyvinylidene fluoride (PVDF) metallized piezo film sheets, and polydimethylsiloxane (PDMS). The lower layer is the substrate layer for supporting and also acts as a friction layer, which is composed of silicone and silver nanowires (AgNWs). The SEM images of the structure of the two layers are shown in the middle of Fig. 1b. The parallel strip-shaped power generation units mimic the gill cleft structure of sharks. The PDMS at the bottom of the strip is similar to the gill arch cartilage, which mainly supports the strip structure. The PVDF in the middle of the strip is equivalent to the gill filament, which is the core component for electricity conversion. The silicone on both sides of the strip-shaped power generation units is like gill muscles, which effectively connects the strips with the substrate layer and regulates the shape of the strips when stretching. In a working cycle, multiple strip-shaped power generation units will deform synchronously and generate the synchronous electrical response.

3.2. Mechanical analysis of bionic shark gill structure

To understand the mechanism of the spontaneous arching upward of the strips in the BSG structure during stretching, we have made a primary mechanical analysis of the elastic deformation process (Fig. 2a). Suppose the long axis direction of the BSG structure is the x-axis, the short axis direction of the structure is the y-axis, and the thickness direction of the structure is the z-axis. When tension from the x-axis direction is applied to both ends of the structure, the entire structure will elongate along the x-axis direction. The Poisson's ratio of silicone is about 0.5, which is similar to that of incompressible material. Therefore, the entire structure will also be significantly deformed (narrowed) in the y-axis direction, resulting in the pressure on both ends of the strip structure in the upper layer, which makes the strip structure unstable. Due to the discontinuity of the upper layer of the BSG structure, the lower substrate layer is the main part to bear the tensile load. The substrate layer becomes stiffer than the upper layer under the action of tensile load, causing the unstable strip structure in the upper layer

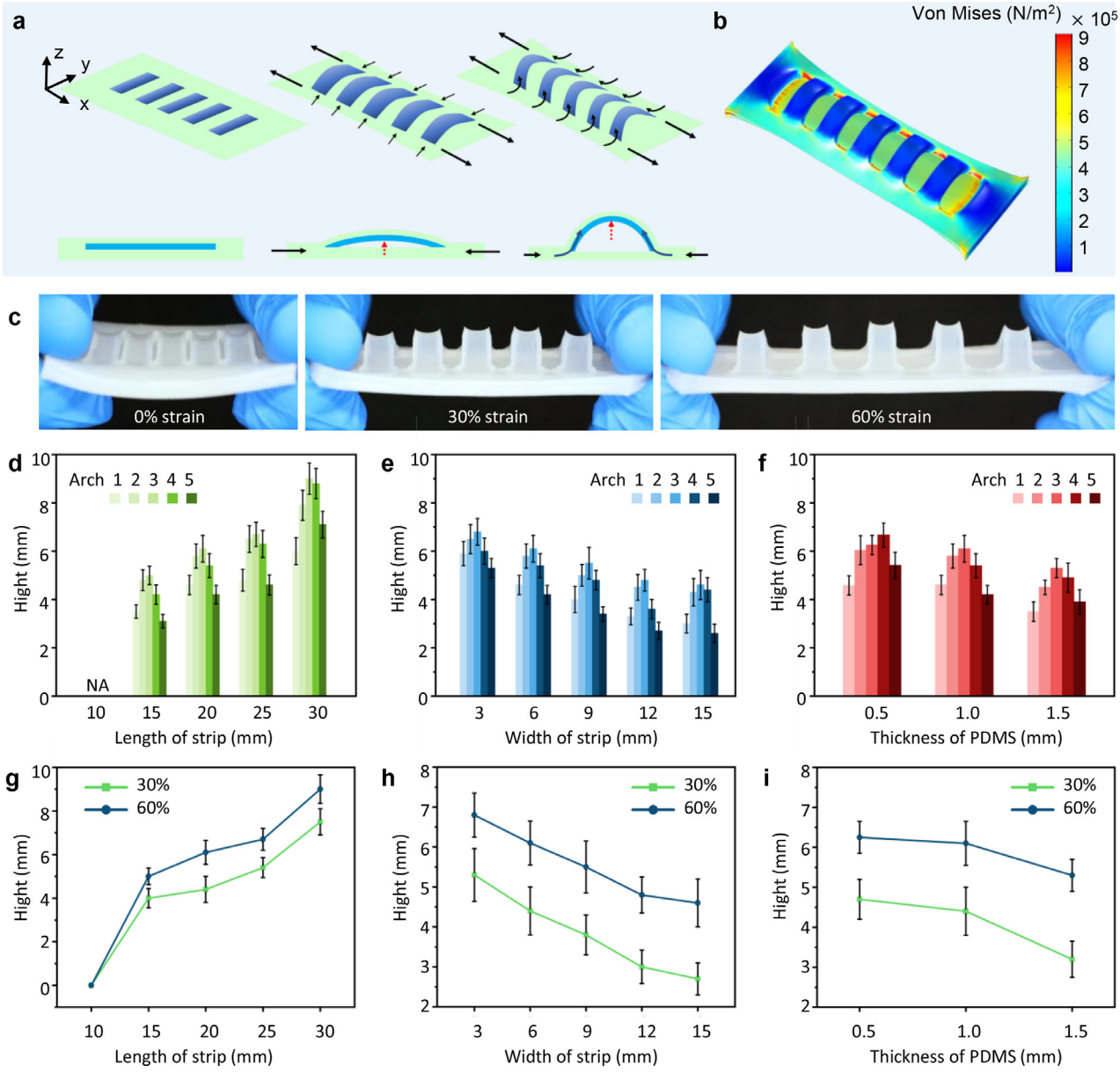

Fig. 2. Elastic deformation and mechanical analysis of the bionic shark gill (BSG) structure during stretching. (a) Mechanical analysis of BSG structure when stretched. (b) Simulation result of BSG structure under 60% strain. (c) Optical photos of BSG structure under 0%,30% and 60% strain. (d-f) Arch height statistics of BSG structures with strips of different lengths, widths, and PDMS thicknesses under 60% strain. (g-i) Arch height statistics of middle strips of BSG structures with different lengths, widths and PDMS thicknesses strips under 30% and 60% strains. All data in (d-i) are presented as the mean ± SD.

to deform along the z-axis direction, thereby arching upward spontaneously.

The overall strain of the BSG structure is continuous according to continuum mechanics, while the stress distribution of each part is different under the same strain due to the difference in Young's modulus. Specifically, the stress of the PDMS layer in strip structure is greater than that of the silicone layer. The surface stress distribution of the BSG structure in the tensile state is verified through a finite element simulation using COMSOL Multiphysics (Fig. 2b). The optical photos of the BSG structure under no stretching, 30% tensile strain and 60% tensile strain are shown in Fig. 2c. The surface stress distribution of the corresponding state through the finite element simulation is shown in Fig. S2. A surface stress dynamic model is also constructed to verify the stability of the BSG structure during stretching (Note S2, Video S1).

Since the pressure from silicone on both ends of the strip is constant when the BSG structure is under the fixed tensile state, the main factors influencing the arching shape depend on the structural features of the strip itself. The strips with different lengths, widths and PDMS layer thicknesses are set as different groups to fabricate BSG structure, respectively. The arching heights of the strips in different groups are counted respectively when the BSG structure is under 60% tensile strain (Fig. 2d-f). The statistical results show that the arching height increases significantly with the increase of the length of the strip. The strips can hardly arch upward when the length of the strip is reduced to 10 mm. In contrast, the arching height decreases with the increase of the width of the strip and the thickness of the PDMS layer. In addition, it is noted that the arching height of the middle strip in the BSG structure is the highest and tends to decrease along both sides. The arching heights of the middle strip of different BSG structures in 30% and 60% tensile states are also counted (Fig. 2g-i). When the tensile strain of the BSG structure increases from 30% to 60%, the arching height of the strip increases significantly. The deformation of the BSG structure along the

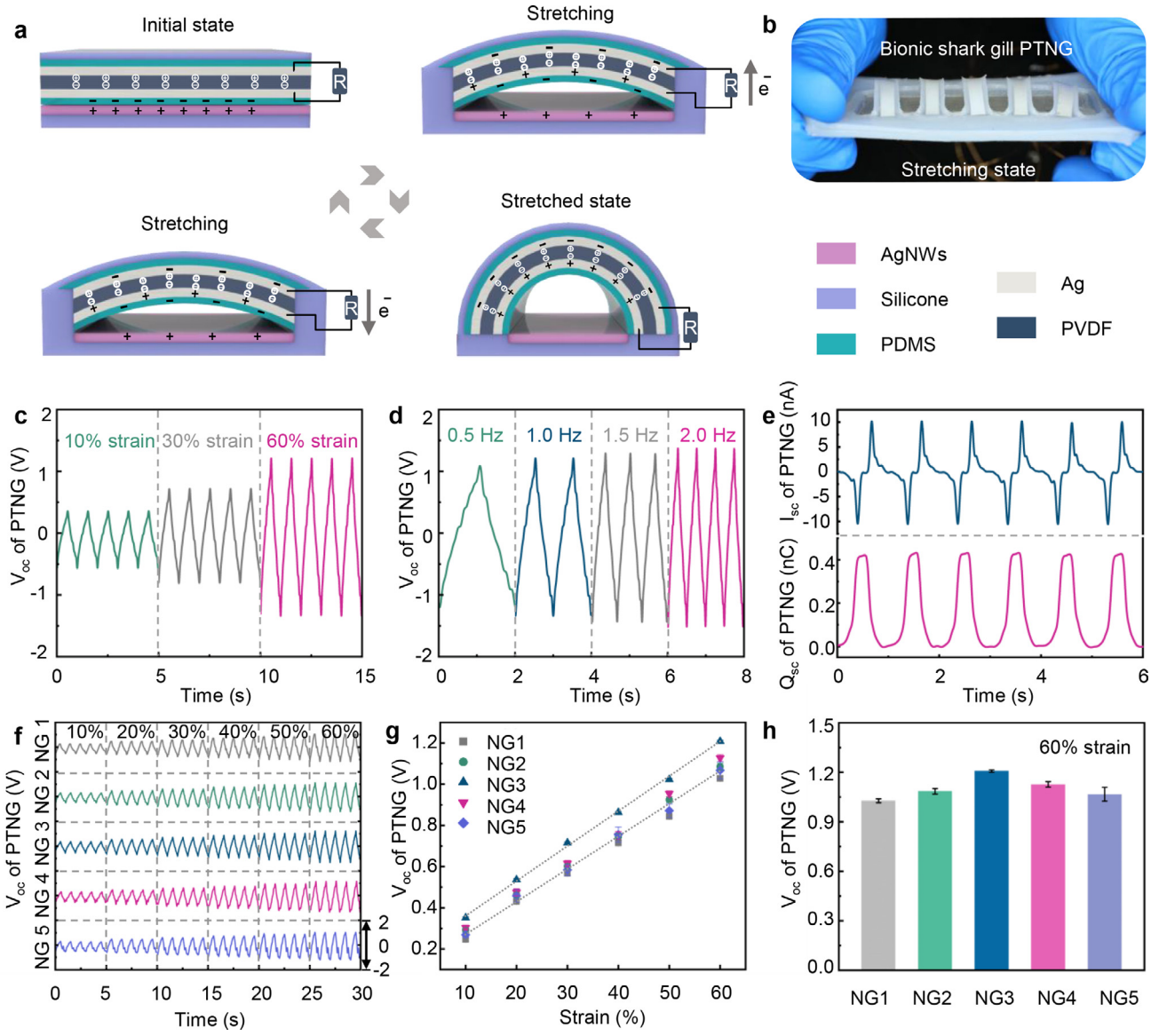

Fig. 3. Working principle and output performance of a bionic shark gill structure piezo-tribo hybrid nanogenerator (BSG-PTNG). (a) Schematic diagram of the working mechanism of BSG-PTNG. (b) Optical photo of BSG-PTNG. (c) Open-circuit voltage of BSG-PTNG under different strains (at 1 Hz). (d) Open-circuit voltage of BSG-PTNG under different working frequencies (60% strain). (e) Short-circuit current and transferred charge of BSG-PTNG (60% strain, at 1 Hz). (f) Open-circuit voltage in multiple channels of BSG-PTNG (10%~60% strain). (g) Voltage response of BSG-PTNG to a range of strains (10%~60%). (h) Peak voltage of BSG-PTNG in multiple channels (60% strain). All data in (g, h) are presented as the mean ± SD.

y-axis direction will increase with the increase of the deformation of the BSG structure along the x-axis direction, which in turn causes the deformation of the BSG structure along the z-axis direction to increase.

3.3. Working principle and characterization of shark gill-like nanogenerator

Based on the elastic deformation mechanism of BSG structure during stretching, a stretchable piezo-tribo hybrid nanogenerator (PTNG) that mimics shark gill is constructed. Each strip in the BSG structure can be prepared into a single PTNG. The working principle of a single PTNG in the BSG structure is shown in Fig. 3a. In the initial state, the stirp in the BSG structure is horizontal, and the power generation unit does not work. When the BSG structure is stretched, the strip bends into an arch and separates from the AgNWs area of the substrate layer. The PVDF film in the strip is compressed to generate piezoelectric polarization charges [30]. Meanwhile, the PDMS layer of the strip and the AgNWs surface of the substrate layer carry triboelectric charges with opposite polarity due to the triboelectric effect [31]. The triboelectric induced charges are generated on the electrode at the bottom of the PVDF film under the electrostatic induction. An electric field is formed between the electrodes on both sides of the PVDF film in the coupling of the piezoelectric polarization charges and the triboelectric induced charges, driving electrons to flow from one electrode to the other through an external circuit [32,33]. When the tension is released, the strip in the BSG structure returns to a horizontal state. The electric field generated by piezoelectric polarization charges and the triboelectric induced charges disappears, causing the electrons to flow back in the opposite direction via the external circuit. The PTNG with BSG structure will produce continuous alternating current output in such a working cycle. The optical photo of PTNG with BSG structure is shown in Fig. 3b.

A linear motor is used to apply periodic tension to the nanogenerator with BSG structure along the long axis. The output open-circuit voltage (V_{OC}) of the BSG-PTNG in single channel under different tensile strains and different operating frequencies are shown in Fig. 3c and d, respectively. When the operating frequency is 1 Hz, the V_{OC} of the BSG-

PTNG is ~0.35 V, ~0.71 V, ~1.21 V under 10%, 30%, 60% tensile strain. The output V_{OC} of BSG-PTNG increases significantly with the increase of tensile strain. When under 60% tensile strain, the V_{OC} of the BSG-PTNG is ~1.08 V, ~1.21 V, ~1.29 V, ~1.36 V at operating frequencies of 0.5 Hz, 1 Hz, 1.5 Hz, 2 Hz, respectively. The output V_{OC} of BSG-PTNG increases slightly with the increase of the operating frequency. When BSG-PTNG is under 60% tensile strain and at 1 Hz operating frequency, the output short-circuit current (I_{SC}) and short-circuit charge transfer (Q_{SC}) of BSG-PTNG is ~10.17 nA and ~0.43 nC, respectively (Fig. 3e). The nanogenerator with BSG structure based on piezoelectric unit alone and triboelectric unit alone is also constructed and characterized. The corresponding working principle and output performance of PENG and TENG with BSG structure is shown in Figs. S3, S4 and Notes S3, S4. It can be found that the output of PTNG with BSG structure is improved compared to PENG or TENG alone. This may be attributed to the fact that the PENGs mainly respond to the changes in the stress loaded on the piezoelectric materials, while the TENGs mainly respond to the relative displacement between the friction layers during the deformation process [34]. The response characteristics of PENG and TENG can be complementary in a hybrid way, which leads to an improvement of output performance of the hybrid PTNG as a sensor [35–37].

The V_{OC} in multiple channels of BSG-PTNG under different strains is shown in Fig. 3f, each channel shows a similar electrical response. The voltage response of BSG-PTNG is approximately linear over a strain range of 10% to 60% (Fig. 3g). It is worth noting that the peak V_{OC} of different channels of BSG-PTNG is slightly different, taking 60% strain as an example, shown in Fig. 3h. This is mainly caused by the slight difference in deformation of the power generation units during stretching.

3.4. Bionic shark gill respiratory sensor

Although humans and sharks breathe in different ways, there are also some commonalities (Fig. S5). The respiration of the human body is accompanied by the contraction and relaxation of the diaphragm and intercostal muscles, which in turn leads to changes in chest circumference or abdominal circumference. The respiration of sharks is accompanied by the contraction and relaxation of gill muscles, which regulates the morphological changes of the gill pouch and gill arches in the gill cleft. The output V_{OC} of the nanogenerator with BSG structure is positively correlated with the tensile strain, which can be used to perceive changes in the human body's abdominal circumference or chest circumference. The sensing of respiratory movement can be realized by converting the mechanical energy in the respiration process into electrical signals. Most of the existing respiratory sensors have only a single channel; the respiratory frequency and respiratory depth are extracted from the respiratory signals collected by a single sensing unit. The single-channel respiratory sensor may be affected by many factors, such as fixed position, displacement of the device during the test, and movement from other parts of the body. The nanogenerator with BSG structure can serve as a multichannel respiratory sensor because each strip in the BSG structure can be prepared into an independent sensing unit.

Differentiated response characteristic will endow the sensor with more selectivity. From the mechanical analysis of the BSG structure, we know that the deformation of the middle strip is slightly greater than that of the strips on both sides when the BSG structure is stretched. The difference is also reflected in the power generation units prepared with BSG structure. Here an optimized BSG structure with strip length decreasing from the middle to the sides is designed to enlarge the deformation difference of the strips under tensile state. The optimized BSG structure exhibits graded response to different tensile strains, as shown in Fig. 4a. When the tensile strain is small, only the strips in the middle respond to bend and arch upward. As the tensile strain increases, the strips at the edge bend and arch upward by degrees. The schematic diagram and optical photo of a stretchable seven-channel respiratory sensor based on optimized BSG structure are shown in Fig. 4b and c, respectively. The output V_{OC} of the seven channels of the bionic shark gill respiratory sensor (BSG-RS) under different tensile strains (10% to 60%, 1 Hz operating frequency) is shown in Fig. 4d, the overall output V_{OC} of BSG-RS increases with the tensile strain. It is worth noting that the V_{OC} of the channels at different positions also exhibits graded electrical response to different tensile strains (Fig. 4e). The third, fourth and fifth channels in the middle position of BSG-RS always show strong and approximate linear electrical response in the range of 10% to 60% tensile strain. The second and sixth channels near the edge of BSG-RS show well electrical response in the range of 20% to 60% tensile strain, while the electrical response under 10% to 20% tensile strain is weak. The first and seventh channels at the most edge of the BSG-RS only exhibit obvious electrical response in the range of 40% to 60% tensile strain. The sensitivity of each channel of BSG-RS can be defined as $= \frac{\Delta V}{\Delta \varepsilon}$, where ΔV is the relative change in output voltage of each channel and $\Delta \varepsilon$ is the relative change of the tensile strain of BSG-RS in long axis direction. The sensitivity and linearity of each channel of BSG-RS separately over the strain range of significant electrical response is shown in Table S1. The middle channel of BSG-RS has a highest sensitivity with a slope of 0.02012, since the length of BSG-RS is 90 mm, the sensitivity can also be converted into 0.02236 V/mm. The comparison of BSG-PTNG based on BSG structure and BSG-RS based on optimized BSG structure under different tensile strains are shown in Fig. S6. The optical photos and normalized output V_{OC} in each channel show that the optimized BSG structure can significantly amplify the deformation difference of the strip power generation units under tensile strain and exhibit distinct graded electrical response to different strains. Taking use of the graded electrical response of BSG-RS to different tensile strains, the abdominal or chest circumference changes during breathing can be monitored accurately, and the respiratory depth can be reflected accordingly.

The output V_{OC} of the seven channels of BSG-RS at different operating frequencies (0.5 Hz, 1 Hz, 1,5 Hz, 2 Hz, 60% tensile strain) is shown in Fig. 4f. It can be seen that the overall output V_{OC} of BSG-RS does not change significantly with the change of operating frequency, indicating that the operating frequency has little influence on the signal intensity of BSG-RS. Therefore, the respiratory rate and respiratory depth of the human body can be monitored accurately and simultaneously by BSG-RS. The stress-strain curve of BSG-RS under tension is shown in Fig. S7. The BSG-RS requires less than 3 N force when stretched to 60% strain and about 1.5 N force when stretched to 30% strain. Such a mechanical load is relatively small for the human body. Therefore BSG-RS does not impose an excessive burden on the human body when used in respiratory monitoring. The durability and stability of the sensor are essential for long-term monitoring of human respiratory movement. Here a linear motor is used to apply long-term mechanical traction (30% tensile strain, 1.3 Hz) to the BSG-RS for fatigue testing. The output V_{OC} of BSG-RS throughout 50,000 working cycles is shown in Fig. 4g. The output V_{OC} of BSG-RS in seven channels has almost no attenuation after 50,000 working cycles (Fig. S8). By comparing the cyclic stress-strain curves of BSG-RS before and after fatigue testing (Fig. S9), the stretchability and elasticity of the device are almost unchanged, indicating that BSG-RS has good stability and fatigue resistance. The comparison of BSG-RS with similar self-powered respiratory sensors is shown in Table S2.

3.5. Wireless real-time respiratory monitoring and analysis system

By integrating BSG-RS with an OpenBCI data acquisition module and a supporting software written by Python, a wearable wireless real-time respiratory monitoring and analysis system based on BSG-RS is developed (Fig. 5a). The block diagram of the entire system is shown in Fig. S10. The software interface of the system can display the real-time respiratory waveform, average respiratory rate, and visualized respiratory intensity (Fig. 5b). By extracting data from multiple channels of BSG-RS, combined with a pattern recognition algorithm, the breathing state can be comprehensively judged. Fig. 5c, d shows the state of a subject wearing the system on the waist when inhaling and exhaling, respectively. To test the effect of the system in respiration monitoring, the res-

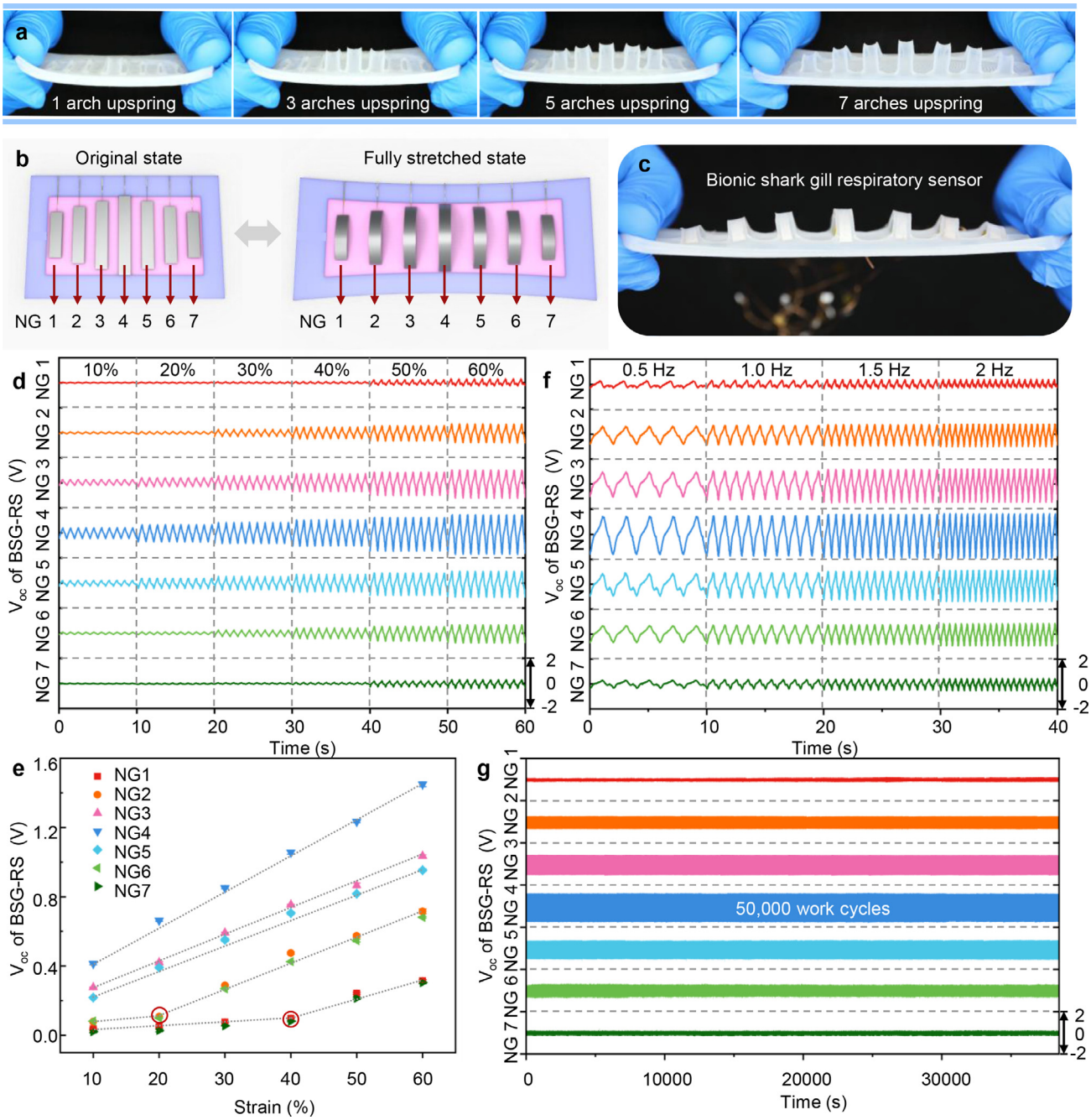

Fig. 4. Characterization of multichannel respiratory sensor based on optimized bionic shark gill structure. (a) Optical photos of the optimized BSG structure under different strains. (b) Schematic diagram of the seven-channel BSG-RS. (c) Optical photo of a seven-channel BSG-RS under stretched state. (d) Open-circuit voltage of BSG-RS under different strains (at 1 Hz). (e) Voltage response of BSG-RS to a range of strains (10%~60%). (f) Open-circuit voltage of BSG-RS at different working frequencies (60% strain). (g) Open-circuit voltage of BSG-RS throughout 50,000 working cycles (50% strain, at 1.3 Hz). All data in (e) are presented as the mean ± SD.

piratory waveforms of the subject under three different breathing states were recorded (Fig. 5e-g). For short and shallow breathing state, only the respiratory waveforms of the middle three channels (C3-C5) are apparent. For normal breathing state, except for the two most marginal channels, the respiratory waveforms of other channels (C2-C6) are apparent. For long and deep breathing state, the respiratory waveforms recorded by all channels (C1-C7) are apparent. The abdominal circumference changes little when breathing is shallow, and the BSG-RS fixed on the waist is stretched less, only the power generation units close to the middle area are driven effectively. As the breathing depth increases, the change in the abdominal circumference will increase significantly, causing the BSG-RS to be further stretched so that more power generation units are effectively driven. Therefore, the respiratory depth can be comprehensively estimated through the respiratory waveforms recorded by multiple channels based on the graded electrical response of BSG-RS.

Respiratory status can reflect the features of some diseases to a certain extent, so the detection of respiratory status is of great significance for remote assisted medical diagnosis. By setting the corresponding response threshold for each channel and using the pattern recognition algorithm, the breathing state can be effectively recognized by analyzing the respiratory signals collected in a period. The complete process is shown in Video S2. The comparison of the respiratory waveform recorded by BSG-RS and a commercial respiratory sensor (MP150, Biopac Systems) is shown in Fig. 5h. P-P interval is the time between two

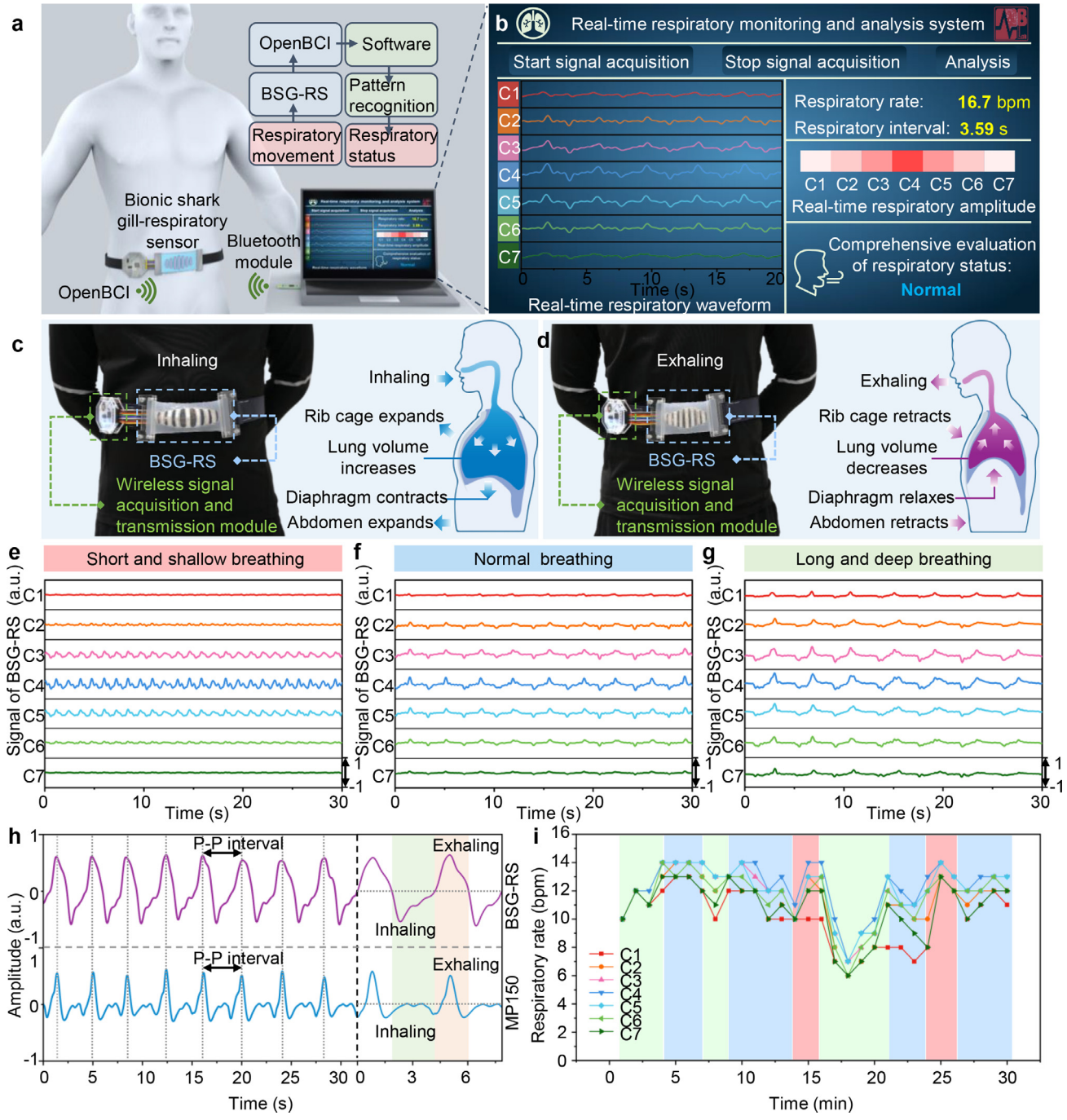

Fig. 5. Wireless real-time respiratory monitoring and analysis system based on BSG-RS. (a) Schematic diagram of the whole system. (b) Software interface of the system. (c,d) Optical photos of the subject wore BSG-RS when inhaling and exhaling, respectively. (e-g) Respiratory physiological signals collected by BSG-RS and recorded by the system under different breathing states. (h) Comparison of respiratory waveforms recorded by BSG-RS and a commercial respiratory sensor. (i) Respiratory rate recorded by BSG-RS over a period of time (30 mins).

consecutive peaks of the signals recorded by respiratory sensor, which can be taken as a respiratory cycle and calculate the respiratory rate. Take the respiratory waveform recorded by MP150 as the standard respiratory waveform, the accuracy (A) of the respiratory rate monitoring can be defined as the degree of closeness of the P-P interval of BSG-RS (PP_{BSG}) to the P-P interval of MP150 (PP_{MP150}), which can be expressed as:

$$A = \left(1 - \frac{|PP_{BSG} - PP_{MP150}|}{PP_{MP150}}\right) \times 100\%$$

The accuracy of BSG-RS reached ~ 98.6% by statistical calculation, demonstrating an accurate respiratory monitoring function of BSG-RS. In addition, the respiration waveform recorded by BSG-RS can more obviously reflect the waveform signals of the inhalation and exhalation stages compared with the commercial respiratory sensor. The inhalation and exhalation stages of a respiratory cycle can be easily identified according to the peak and valley phases of the respiratory waveform from the BSG-RS.

The respiratory signals of the subject were recorded during a period of time (30 minutes), and the respiratory rates recorded by different channels during the period were counted by software (Fig. 5i). Compared with the traditional single-channel respiratory sensor, multiple channels of BSG-RS can better reflect the changing trend of respiratory rate within a period of time, so as to avoid the omission or over-counting

of the single-channel sensor due to the interference from other factors. To verify the anti-interference ability of BSG-RS, we tested the performance of BSG-RS for respiratory monitoring when disturbed by limb movements, and compared it with the commercial respiratory sensor MP150, as shown in Fig. S11. BSG-RS can simultaneously record interference signals and normal respiratory signals unaffected by interference through different channels. By comparing and analyzing the respiratory signals recorded in multiple channels of BSG-RS, we can effectively identify physiological parameters such as respiratory rate and respiratory intensity even with some interference from external factors, and even could make a simple discrimination of the interference signals according to the channels in which interference signals are recorded (such as interference from the left or right side of the body).

The BSG-RS worn on the waist could also obtain clear respiratory waveform signals when the subject was sitting and lying, respectively (Fig. S12). Noise interference from exercise is a common problem for wearable sensors. In addition to static conditions, the performance of BSG-RS for respiratory monitoring under exercise was also tested. As shown in Fig. S13, when the subject was walking, the BSG-RS could still acquire legible respiratory waveform signals, while when the subject was jogging, the acquired respiratory signals were accompanied by obvious noise signals, and only the middle several channels (C3-C5) could distinguish the respiratory waveform signals. The breathing method of the human body mainly has two types of thoracic breathing and abdominal breathing (Fig. S14). In daily life, people can switch between these two breathing methods as needed. We fixed the BSG-RS to the chest and abdomen of another subject for respiratory monitoring, respectively. The respiratory physiological signals of the subject in both types of adopting thoracic and abdominal breathing could be well captured by the BSG-RS (Fig. S15), which further verifying the general applicability of the BSG-RS.

4. Conclusion

In summary, inspired by the tissue structure of the shark gill cleft, we designed a bionic shark gill structure, which can spontaneously convert the transverse elastic deformation into the longitudinal elastic deformation when it is stretched. Based on this feature, a stretchable nanogenerator with multiple channels has been successfully constructed. A multichannel respiratory sensor based on bionic shark gill structure is fabricated through further structure optimization, which can produce graded electrical responses to different tensile strains. The BSG-RS can achieve the simultaneous detection of human respiratory rate and respiratory depth. In addition, a wireless real-time respiratory monitoring and analysis system is constructed based on BSG-RS to realize the monitoring of human respiratory movement under various postures. Different breathing states can be identified effectively through further analysis of the recorded respiratory signals by supporting software. The respiratory sensing system based on BSG-RS has a core sensing component conformal matching with human tissues, and the bionic design of multiple channels makes it have a certain anti-interference ability, good stability and durability under long-term testing. In the future, the noise impact of the exercise may be reduced by employing some efficient noise reduction algorithms or by optimizing the fabrication process to miniaturize BSG-RS and fit the human skin directly and tightly. With the rapid development of machine learning and artificial intelligence [38,39], it is expected to be applied as a home health care system and remote auxiliary diagnosis tool for respiratory diseases.

Data availability statement

All data needed to evaluate the conclusions in the paper are present in the paper and/or the Supporting Information. Additional data related to this paper may be requested from the authors.

Declaration of Competing Interest

The authors declare that they have no conflicts of interest tin this work.

Acknowledgments

The authors thank the National Natural Science Foundation of China (Grants No. T2125003, 61875015, and 62004010), Beijing Natural Science Foundation (Grants No. JQ20038 and 7204275), and The Fundamental Research Funds for the Central Universities for the support.

Supplementary materials

Supplementary material associated with this article can be found, in the online version, at doi:10.1016/j.fmre.2022.01.003.

References

[1] M. Xie, X.S. Liu, X.P. Cao, et al., Trends in prevalence and incidence of chronic respiratory diseases from 1990 to 2017, Resp. Res. 21 (1) (2020) 1–13.
[2] G. Viegi, S. Maio, S. Fasola, et al., Global Burden of Chronic Respiratory Diseases, J. Aerosol. Med. Pulm. D. 33 (4) (2020) 171–177.
[3] N.R. Zhang, L.L. Wang, X.Q. Deng, et al., Recent advances in the detection of respiratory virus infection in humans, J. Med. Virol. 92 (4) (2020) 408–417.
[4] D.E. Becker, A.B. Casabianca, Respiratory monitoring: physiological and technical considerations, Anesth. Prog. 56 (1) (2009) 14–22.
[5] P. Måseide, Body work in respiratory physiological examinations, Sociol. Health Ill. 33 (2) (2011) 296–307.
[6] M. Sarkar, I. Madabhavi, N. Niranjan, et al., Auscultation of the respiratory system, Ann. Thorac. Med. 10 (3) (2015) 158–168.
[7] Y. Khan, A.E. Ostfeld, C.M. Lochner, et al., Monitoring of Vital Signs with Flexible and Wearable Medical Devices, Adv. Mater. 28 (22) (2016) 4373–4395.
[8] Y.J. Su, G.R. Chen, C.X. Chen, et al., Self-Powered Respiration Monitoring Enabled By a Triboelectric Nanogenerator, Adv. Mater. 33 (35) (2021) 2101262.
[9] J. Dai, L. Li, B. Shi, et al., Recent progress of self-powered respiration monitoring systems, Biosens. Bioelectron. 195 (2021) 113609.
[10] C. Massaroni, A. Nicolo, E. Schena, et al., Remote Respiratory Monitoring in the Time of COVID-19, Front. Physiol. 11 (2020) 635.
[11] W. Taylor, Q.H. Abbasi, K. Dashtipour, et al., A Review of the State of the Art in Non-Contact Sensing for COVID-19, Sensors-Basel 20 (19) (2020) 5665.
[12] H. Jeong, J.A. Rogers, S. Xu, Continuous on-body sensing for the COVID-19 pandemic: Gaps and opportunities, Sci. Adv. 6 (36) (2020) eabd4794.
[13] Q. Zheng, B.J. Shi, Z. Li, et al., Recent Progress on Piezoelectric and Triboelectric Energy Harvesters in Biomedical Systems, Adv. Sci. 4 (7) (2017) 1700029.
[14] H.Q. Feng, C.C. Zhao, P.C. Tan, et al., Nanogenerator for Biomedical Applications, Adv. Healthc. Mater. 7 (10) (2018) 1701298.
[15] Y.H. Jung, S.K. Hong, H.S. Wang, et al., Flexible Piezoelectric Acoustic Sensors and Machine Learning for Speech Processing, Adv. Mater. 32 (35) (2020) 1904020.
[16] D.S. Liu, H. Ryu, U. Khan, et al., Piezoionic-powered graphene strain sensor based on solid polymer electrolyte, Nano Energy 81 (2021) 105610.
[17] Z. Liu, S. Zhang, Y.M. Jin, et al., Flexible piezoelectric nanogenerator in wearable self-powered active sensor for respiration and healthcare monitoring, Semicond. Sci. Tech. 32 (6) (2017) 064004.
[18] Z.C. Zhang, J.W. Zhang, H. Zhang, et al., A Portable Triboelectric Nanogenerator for Real-Time Respiration Monitoring, Nanoscale Res. Lett. 14 (1) (2019) 1–11.
[19] Z.Z. Zhao, C. Yan, Z.X. Liu, et al., Machine-Washable Textile Triboelectric Nanogenerators for Effective Human Respiratory Monitoring through Loom Weaving of Metallic Yarns, Adv. Mater. 28 (46) (2016) 10267–10274.
[20] S.W. Chen, N. Wu, L. Ma, et al., Noncontact Heartbeat and Respiration Monitoring Based on a Hollow Microstructured Self-Powered Pressure Sensor, Acs Appl. Mater. Inter. 10 (4) (2018) 3660–3667.
[21] F. Yi, L. Lin, S.M. Niu, et al., Stretchable-Rubber-Based Triboelectric Nanogenerator and Its Application as Self-Powered Body Motion Sensors, Adv. Funct. Mater. 25 (24) (2015) 3688–3696.
[22] X. Peng, K. Dong, C.Y. Ye, et al., A breathable, biodegradable, antibacterial, and self-powered electronic skin based on all-nanofiber triboelectric nanogenerators, Sci. Adv. 6 (26) (2020) eaba9624.
[23] J. Li, Y. Long, F. Yang, et al., Respiration-driven triboelectric nanogenerators for biomedical applications, EcoMat 2 (3) (2020) e12045.
[24] W.J. Fan, Q. He, K.Y. Meng, et al., Machine-knitted washable sensor array textile for precise epidermal physiological signal monitoring, Sci. Adv. 6 (11) (2020) eaay2840.
[25] X. Peng, K. Dong, C.A. Ning, et al., All-Nanofiber Self-Powered Skin-Interfaced Real-Time Respiratory Monitoring System for Obstructive Sleep Apnea-Hypopnea Syndrome Diagnosing, Adv. Funct. Mater. 31 (34) (2021) 2103559.
[26] H.Y. Guo, X.J. Pu, J. Chen, et al., A highly sensitive, self-powered triboelectric auditory sensor for social robotics and hearing aids, Sci. Robot. 3 (20) (2018).
[27] H. Zhou, D.X. Li, X.M. He, et al., Bionic Ultra-Sensitive Self-Powered Electromechanical Sensor for Muscle-Triggered Communication Application, Adv. Sci. 8 (15) (2021) 2101020.
[28] G. De Iuliis, D. Pulerà, The dissection of vertebrates, Academic press, 2019.

[29] A.P. Klimley, The biology of sharks and rays, University of Chicago Press, 2013.
[30] Z.L. Wang, On Maxwell's displacement current for energy and sensors: the origin of nanogenerators, Mater. Today. 20 (2) (2017) 74–82.
[31] C.S. Wu, A.C. Wang, W.B. Ding, et al., Triboelectric Nanogenerator: A Foundation of the Energy for the New Era, Adv. Energy Mater. 9 (1) (2019) 1802906.
[32] J.G. Sun, T.N. Yang, C.Y. Wang, et al., A flexible transparent one-structure tribo-piezo-pyroelectric hybrid energy generator based on bio-inspired silver nanowires network for biomechanical energy harvesting and physiological monitoring, Nano Energy 48 (2018) 383–390.
[33] K. Dong, X. Peng, Z.L. Wang, Fiber/Fabric-Based Piezoelectric and Triboelectric Nanogenerators for Flexible/Stretchable and Wearable Electronics and Artificial Intelligence, Adv. Mater. 32 (5) (2020) 1902549.
[34] Y. Zou, J.W. Liao, H. Ouyang, et al., A flexible self-arched biosensor based on combination of piezoelectric and triboelectric effects, Appl. Mater. Today. 20 (2020) 100699.
[35] X.X. Chen, Y. Song, Z.M. Su, et al., Flexible fiber-based hybrid nanogenerator for biomechanical energy harvesting and physiological monitoring, Nano Energy 38 (2017) 43–50.
[36] Y.B. Guo, X.S. Zhang, Y. Wang, et al., All-fiber hybrid piezoelectric-enhanced triboelectric nanogenerator for wearable gesture monitoring, Nano Energy 48 (2018) 152–160.
[37] J.B. Yu, X.J. Hou, M. Cui, et al., Highly skin-conformal wearable tactile sensor based on piezoelectric-enhanced triboelectric nanogenerator, Nano Energy 64 (2019) 103923.
[38] F. Wen, Z.D. Sun, T.Y.Y. He, et al., Machine Learning Glove Using Self-Powered Conductive Superhydrophobic Triboelectric Textile for Gesture Recognition in VR/AR Applications, Adv. Sci. 7 (14) (2020) 2000261.
[39] M.L. Zhu, Z.D. Sun, Z.X. Zhang, et al., Haptic-feedback smart glove as a creative human-machine interface (HMI) for virtual/augmented reality applications, Sci. Adv. 6 (19) (2020) eaaz8693.

Yang Zou received his Bachelor's degree from Beihang University in 2016, and Doctor's Degree in Nanoscience and Technology from University of Chinese Academy of Sciences in 2021. He is now a postdoctoral fellow at the Beijing Institute of Technology. His research interests mainly focus on soft energy harvesters and biosensors, nanogenerators and bionic electronics.

Zhou Li received his Bachelor's degree from Wuhan University in 2004, and Doctor's Degree from Peking University in 2010. He joined School of Biological Science and Medical Engineering of Beihang University in 2010 as an associate Professor. Currently, he is principal investigator and group leader of Nanoenergy and Biosystem Lab (NBL) in Beijing Institute of Nanoenergy and Nanosystems, Chinese Academy of Sciences. He is supported by the National Youth Talent Support Program and the National Science Fund for Distinguished Young Scholars. His research interests include nanogenerators, in vivo energy harvesters and self-powered medical devices, biosensors.